

NUMERICAL SIMULATION OF HYPERSONIC PLASMA FLOW BASED ON NONLINEAR COUPLED CONSTITUTIVE RELATIONS

Hao Shi[1], Chenchen Song[1] & Hong Xiao[1]

[1]School of Power and Energy, Northwestern Polytechnical University, Xi'an 710072, China

Abstract

Magnetohydrodynamic (MHD) thermal protection provides an active means of modifying the shock-layer structure during hypersonic entry. To account for rarefaction effects and real-gas nonequilibrium in weakly ionized air, a finite-volume method coupling the multicomponent nonlinear coupled constitutive relation (NCCR) with MHD source terms is developed under the low-magnetic-Reynolds-number approximation. The NCCR model replaces the conventional Navier–Stokes–Fourier linear closure for stress and heat flux, while Park's two-temperature model and an 11-species finite-rate air mechanism describe thermochemical nonequilibrium. The electromagnetic coupling is introduced through the scalar electric-potential equation, Ohm's law, Lorentz-force source terms, and electromagnetic work. The solver is assessed using OREX reference data, for which the pressure field and stagnation-line temperature profiles agree well with the reported results. The method is then applied to MHD thermal protection of the RAM-C II configuration, with emphasis on the effects of stagnation-point magnetic flux density B_0 and flight altitude H. At $H = 50$ km and $M_\infty = 20$, increasing B_0 from 0 to 2.5 T increases the bow-shock standoff distance to 12.65 times the zero-field value and reduces the stagnation-point heat flux by 38.01%. The heat-flux reduction is accompanied by increased shoulder heating, indicating that reattachment heating limits the benefit of further increasing magnetic flux density. For $B_0 = 1$ T, the stagnation-point heat-flux reduction increases with altitude, from 0.05% at 30 km to 67.86% at 70 km. These results show that MHD thermal-protection performance is governed not only by magnetic-field strength, but also by shock-layer ionization, current localization, and heat-load redistribution over the forebody.

Keywords: Hypersonic flow; Rarefied flow; Weakly ionized plasma; MHD thermal protection; Nonlinear coupled constitutive relations

1. Introduction

During hypersonic atmospheric reentry, a substantial fraction of the freestream kinetic energy is deposited in the detached shock layer ahead of the vehicle, producing a steep rise in post-shock temperature. The resulting aerothermodynamic environment involves vibrational excitation, molecular dissociation, partial ionization, strong transport-property variations, and intense wall heat transfer [1–3]. Classical stagnation-point theory shows that the stagnation-point heat flux is sensitive to boundary-layer transport, wall catalysis, and high-temperature chemistry [4]. For high-enthalpy entry, the thermal-protection problem is therefore coupled to the shock-layer structure, including the bow-shock standoff distance, thermochemical relaxation, ionization level, and transport fluxes between the shock and the wall.

Current thermal protection systems (TPS) for high-speed vehicles rely mainly on passive approaches, such as ablative protection, reusable insulation, high-temperature structural materials, and surface-catalysis control. Passive thermal protection is reliable, but once the vehicle geometry, reentry trajectory, and material system are fixed, its response to the entry thermal environment is largely prescribed. Active thermal protection instead modifies the near-wall flow structure and, in turn, the

aerothermal environment. It acts on the shock-layer structure and near-wall transport before the high-temperature post-shock gas reaches the wall. A typical example is counterflow injection, which pushes the bow shock away from the vehicle surface and thereby reduces aerodynamic heating at the wall [5]. Under high-enthalpy reentry conditions, the high-temperature air behind the detached shock may become weakly ionized and exhibit finite electrical conductivity, allowing an imposed electromagnetic field to act directly on the shock-layer gas. Magnetohydrodynamic (MHD) thermal protection uses an applied magnetic field to act on this high-temperature ionized air; the resulting Lorentz force modifies the flow structure and reduces aerodynamic heating on the vehicle surface.

At the flow-physics level, MHD thermal protection relies on the finite electrical conductivity of the shock layer. The imposed magnetic field induces a current through the motional electromotive term, and the resulting Lorentz force extracts momentum from the conducting post-shock gas. The bow shock is displaced upstream, the residence time and thermochemical relaxation path are altered, and part of the heat-transfer route to the wall is redistributed. This mechanism traces back to Bush's blunt-body analysis and was later examined in hypersonic MHD simulations and OREX reentry calculations, where the heat-flux reduction was found to depend strongly on natural ionization and current generation in the shock layer [6–8]. Recent studies have extended the problem to ablating surfaces, expansion-tube measurements, imposed-field modeling, reduced stagnation-line descriptions, high-enthalpy shock-wave/boundary-layer interaction, planetary-entry configurations, magnetic shielding, and laboratory plasma manipulation [9–16]. A recurring conclusion is that magnetic-field strength alone is an incomplete design parameter. The effective response is set by the spatial overlap among electron number density n_e, electrical conductivity σ, induced current density $\mathbf{J}$, and the magnetic field, together with the redistribution of Lorentz-force work, Joule heating, and wall heat flux.

In addition, rarefaction and nonequilibrium effects cannot be neglected during high-altitude, high-Mach-number flight. Within the shock layer, some regions may remain close to the continuum regime, whereas others exhibit large gradients, elevated local Knudsen numbers, and clear departures from translational, vibrational, and chemical equilibrium [17, 18]. The direct simulation Monte Carlo (DSMC) method introduced by Bird can accurately describe rarefied nonequilibrium flows, but it becomes computationally inefficient for multidimensional reacting MHD flows near the continuum limit. The nonlinear coupled constitutive relation (NCCR), developed by Eu, Myong, and co-workers, is derived from generalized hydrodynamics and thermodynamically consistent moment closure. It provides an extension within the continuum framework, reduces to the Navier–Stokes–Fourier (NSF) equations near thermodynamic equilibrium, and improves the description of rarefied hypersonic nonequilibrium flows [19–25]. Coupling the NCCR transport model with ionized-air chemistry and the reduced Maxwell equations gives a unified numerical framework for examining how nonequilibrium transport affects MHD heat-flux mitigation.

In this work, an NCCR-MHD solver is developed for hypersonic weakly ionized air plasma flows and applied to the MHD thermal protection of a blunt reentry body. The study clarifies the underlying control mechanism, including the coupled response among shock displacement, two-temperature thermochemistry, n_e redistribution, $\mathbf{J}$ localization, Lorentz-force braking, Joule heating, and wall heat flux. The main contributions are as follows:

1. A multicomponent NCCR-MHD formulation is established for chemically reacting, thermally nonequilibrium, weakly ionized air under the low-magnetic-Reynolds-number approximation.

2. A finite-volume coupling procedure is developed for the gas dynamics, local NCCR closure, finite-rate chemistry, σ evaluation, electric-potential solution, $\mathbf{J} \times \mathbf{B}$ forcing, and electromagnetic energy deposition.

3. The OREX case of Fujino and Ishikawa [8] is used for verification; RAM-C II parametric computations are then performed over B_0 and H.

4. The RAM-C II results identify how B_0 and H set the bow-shock standoff, stagnation-point heat-flux reduction, $\mathbf{J}$ localization, and shoulder heat-load redistribution.

Section 2 presents the governing equations and physical models. Section 3 describes the coupled algorithm. Section 4 presents the OREX assessment. Section 5 gives the RAM-C II results and

discussion, including the effects of stagnation-point magnetic flux density B_0 and flight altitude H. Section 6 summarizes the main findings.

2. Governing Equations

2.1 Multicomponent NCCR-MHD system

The reacting gas is represented with Park's 11-species finite-rate air chemistry model, including N_2, O_2, NO, N, O, N_2^+, O_2^+, NO^+, N^+, O^+, and e^-. Thermal nonequilibrium is described using Park's two-temperature model: the translational-rotational energy mode is assigned the temperature T_t, while vibrational energy, electronic excitation, and free-electron energy share the temperature T_v [3, 26]. With these definitions, the conservation equations are written in the compact form

$$\frac{\partial \mathbf{U}}{\partial t} + \nabla \cdot \mathbf{F}^c + \nabla \cdot \mathbf{F}^n = \mathbf{S}^{chem} + \mathbf{S}^{em}, \tag{1}$$

where

$$\mathbf{U} = \begin{bmatrix} \rho \\ \rho \mathbf{u} \\ \rho E \\ \rho_i \end{bmatrix}, \quad \mathbf{F}^c = \begin{bmatrix} \rho \mathbf{u} \\ \rho \mathbf{u}\mathbf{u} \\ (\rho E + p)\mathbf{u} \\ \rho_i \mathbf{u} \end{bmatrix}, \tag{2}$$

and the NCCR transport flux is

$$\mathbf{F}^n = \begin{bmatrix} 0 \\ \sum_{i=1}^{N_s} (\Pi_i + \Delta_i \mathbf{I}) \\ \sum_{i=1}^{N_s} (\Pi_i + \Delta_i \mathbf{I}) \cdot \mathbf{u} + \mathbf{Q} \\ \mathbf{j}_i \end{bmatrix}. \tag{3}$$

Here ρ, $\mathbf{u}$, p, and E denote mixture density, velocity, pressure, and total energy per unit mass, respectively. The variables Π_i, Δ_i, and $\mathbf{Q}$ are the NCCR shear stress, excess normal stress, and total heat flux. Species diffusion is approximated by

$$\mathbf{j}_i = -\rho D_{c,i} \nabla c_i, \tag{4}$$

where $D_{c,i}$ is the effective diffusion coefficient and c_i is the species mass concentration. The source terms are

$$\mathbf{S}^{chem} = \begin{bmatrix} 0 \\ 0 \\ Q_m \\ \dot{\omega}_i \end{bmatrix}, \qquad \mathbf{S}^{em} = \begin{bmatrix} 0 \\ \mathbf{J} \times \mathbf{B} \\ \mathbf{J} \cdot \mathbf{E} \\ 0 \end{bmatrix}. \tag{5}$$

Transport coefficients and mixture thermophysical properties are calculated with empirical correlations and mixture rules commonly used for multicomponent high-temperature air [27–29]. The species production rates $\dot{\omega}_i$ are supplied by the finite-rate chemistry model, and Q_m represents thermochemical energy exchange together with vibrational-electronic energy relaxation [3, 30]. The electromagnetic field acts on the flow equations mainly through the Lorentz force $\mathbf{J} \times \mathbf{B}$ and the electromagnetic work $\mathbf{J} \cdot \mathbf{E}$. In a local reference frame moving with the gas, the Joule-heating term is expressed as

$$Q_J = \mathbf{J} \cdot (\mathbf{E} + \mathbf{u} \times \mathbf{B}), \tag{6}$$

and the sum of mechanical work by the Lorentz force and rest-frame Joule heating is consistent with the total energy source in Eq. (5).

2.2 NCCR closure

In the NSF equations, stress and heat flux are determined from linear relations with the strain-rate tensor and temperature gradient, respectively. The NCCR model abandons this local linear closure and instead employs an algebraic nonlinear closure derived from generalized hydrodynamics and moment methods [19–22]. For individual species or the mixture as a whole, the nonequilibrium flux vector

$$\mathbf{W}_i = (\Pi_i, \Delta_i, \mathbf{Q}_i) \tag{7}$$

is obtained from

$$\mathscr{R}_i(\mathbf{W}_i; \nabla\mathbf{u}, \nabla T_t, T_t, \rho_i) = 0. \tag{8}$$

The residual $\mathscr{R}_i$ represents the coupled dependence of shear stress, excess normal stress, and heat flux on deformation and dissipation. Near local equilibrium it reduces to

$$\Pi_i \to -2\mu_i \mathbf{S}^{(2)}, \qquad \Delta_i \to -\eta_i \nabla\cdot\mathbf{u}, \qquad \mathbf{Q} \to -\lambda\nabla T_t + \sum_{i=1}^{N_s} h_i \mathbf{j}_i, \tag{9}$$

where $\mathbf{S}^{(2)}$ denotes the traceless symmetric part of the velocity-gradient tensor; μ_i, η_i, λ, and h_i are the shear viscosity, bulk viscosity, thermal conductivity, and species enthalpy, respectively. Under nonequilibrium conditions, the nonlinear dissipation factor in $\mathscr{R}_i$ suppresses the sustained growth of stress and heat flux, while coupling shear deformation, compression, and heat transfer. Equation (8) is solved independently in each control volume by a fixed-point iteration initialized with the NSF values from Eq. (9); once the iteration has converged, the resulting fluxes are substituted into Eq. (3).

2.3 Electromagnetic model

Under the low-magnetic-Reynolds-number approximation, the induced magnetic field is neglected relative to the imposed field for the present weakly ionized hypersonic flow, as commonly adopted in reentry MHD thermal protection calculations [8, 9, 31]. The reduced electrodynamic model reads

$$\nabla\cdot\mathbf{J} = 0, \qquad \mathbf{E} = -\nabla\phi, \tag{10}$$

where ϕ is the scalar electric potential. The generalized Ohm's law is written as

$$\mathbf{J} + \beta_e \mathbf{J}\times\mathbf{b} = \sigma(\mathbf{E} + \mathbf{u}\times\mathbf{B}), \tag{11}$$

where σ is the electrical conductivity, β_e is the electron Hall parameter, and $\mathbf{b} = \mathbf{B}/|\mathbf{B}|$. When the Hall effect is neglected, Eq. (11) reduces to

$$\mathbf{J} = \sigma(-\nabla\phi + \mathbf{u}\times\mathbf{B}). \tag{12}$$

Substitution into current conservation yields the electric-potential equation

$$\nabla\cdot[\sigma(-\nabla\phi + \mathbf{u}\times\mathbf{B})] = 0. \tag{13}$$

For an insulating wall, the normal current vanishes, $\mathbf{J}\cdot\mathbf{n} = 0$. A zero-gradient condition is imposed for ϕ at the symmetry axis, and one reference potential is specified to remove the arbitrary constant. After Eq. (13) is solved, $\mathbf{E}$, $\mathbf{J}$, $\mathbf{J}\times\mathbf{B}$, and Q_J are reconstructed and passed to the gas-dynamic update. The imposed magnetic field is prescribed as a dipole. For the RAM-C II cases, the field is

$$\mathbf{B} = B_0 \frac{R_b^2}{r^2}\left[\left(\cos^2\theta - \sin^2\theta\right)\mathbf{e}_x + \sin(2\theta)\mathbf{e}_y\right], \tag{14}$$

where B_0 is the stagnation-point magnetic flux density, R_b is the body radius, and (r,θ) denotes the local polar coordinate.

3. Coupled Solution Procedure

The NCCR-MHD equations are solved using a density-based finite-volume method within the shock-capturing framework commonly adopted for compressible high-speed flows [32–34]. The inviscid fluxes are evaluated with an upwind discretization, while the NCCR transport terms and species diffusion terms are discretized using second-order central differences. The numerical stiffness of the coupled system arises primarily from the strong interdependence among gas dynamics, thermochemistry, transport closure, and electromagnetic effects. In particular, the local flow state determines T_t, T_v, species composition, n_e, and σ, which in turn govern $\mathbf{J}$ and $\mathbf{J}\times\mathbf{B}$. Lorentz forcing and Joule heating then enter the momentum and total energy equations and modify the shock location and the degree of thermal nonequilibrium. The NCCR closure is treated within the same coupled solution procedure, since the stress tensor and heat flux depend on local gradients altered by magnetic-field interaction.

The semi-discrete finite-volume equation in cell Ω_j is written as

$$\frac{d}{dt}\left(\Omega_j \mathbf{U}_j\right)+\mathbf{R}_j^c(\mathbf{U})+\mathbf{R}_j^n(\mathbf{U},\mathbf{W})=\Omega_j\left[\mathbf{S}_j^{chem}(\mathbf{U})+\mathbf{S}_j^{em}(\mathbf{U},\phi)\right], \tag{15}$$

where $\mathbf{R}_j^c$ is the convective residual, $\mathbf{R}_j^n$ contains NCCR stress, NCCR heat flux, and species diffusion, and $\mathbf{W}=(\Pi,\Delta,\mathbf{Q})$ denotes the nonequilibrium constitutive variables. The electromagnetic source depends on the electric potential through

$$\mathbf{S}_j^{em}=\begin{bmatrix}0\\ \mathbf{F}_L\\ Q_{em}\\ 0\end{bmatrix}_j, \qquad \mathbf{F}_L=\mathbf{J}\times\mathbf{B}, \qquad Q_{em}=\mathbf{J}\cdot\mathbf{E}. \tag{16}$$

A Picard-type sub-iteration is used at each pseudo-time level. The fixed-point map is

$$\mathbf{U}^{(s)}\rightarrow\left(\mathbf{W}^{(s)},\sigma^{(s)}\right)\rightarrow\phi^{(s)}\rightarrow\left(\mathbf{J}^{(s)},\mathbf{F}_L^{(s)},Q_{em}^{(s)}\right)\rightarrow\mathbf{U}^{(s+1)}, \tag{17}$$

where s is the coupling sub-iteration index. This arrangement preserves a modular electromagnetic solve while retaining repeated feedback between the MHD source terms and the NCCR gas-dynamic update.

3.1 NCCR update inside the coupling loop

At the beginning of a coupling sub-iteration, primitive variables are reconstructed from $\mathbf{U}^{(s)}$. Mixture pressure p, T_t, T_v, species mass fractions, chemical source terms, transport coefficients, n_e, and σ are updated. Cellwise velocity and T_t gradients provide the input for the local nonlinear constitutive problem

$$\mathscr{R}_i\left(\mathbf{W}_i^{(m)};\nabla\mathbf{u}^{(s)},\nabla T_t^{(s)},\rho_i^{(s)},T_t^{(s)}\right)=0, \tag{18}$$

where m is the local NCCR iteration counter. The NSF stress and heat flux are used as the initial guess. A relaxed fixed-point update is applied,

$$\mathbf{W}_i^{(m+1)}=(1-\alpha_N)\mathbf{W}_i^{(m)}+\alpha_N\mathscr{G}_i\left(\mathbf{W}_i^{(m)}\right), \tag{19}$$

where $\mathscr{G}_i$ is the algebraic NCCR update operator and α_N is a relaxation factor. The local solve stops when

$$\frac{\left\|\mathbf{W}_i^{(m+1)}-\mathbf{W}_i^{(m)}\right\|}{\left\|\mathbf{W}_i^{(m)}\right\|+\varepsilon_N}<\varepsilon_N. \tag{20}$$

The converged Π_i, Δ_i, and $\mathbf{Q}_i$ are used to assemble $\mathbf{R}_j^n$. Because this operation is local to each control volume, the global gas-dynamic matrix remains close to that of the NSF solver.

3.2 Electromagnetic update

During the electromagnetic sub-step, $\sigma^{(s)}$ and $\mathbf{u}^{(s)}$ are held fixed, giving the potential equation

$$\nabla \cdot \left(\sigma^{(s)} \nabla \phi^{(s)} \right) = \nabla \cdot \left[\sigma^{(s)} \left(\mathbf{u}^{(s)} \times \mathbf{B} \right) \right]. \tag{21}$$

The variable-coefficient elliptic equation is solved with $\mathbf{J} \cdot \mathbf{n} = 0$ at the insulating wall. The electric field $\mathbf{E}$ and current density $\mathbf{J}$ are then reconstructed as

$$\mathbf{E}^{(s)} = -\nabla \phi^{(s)}, \qquad \mathbf{J}^{(s)} = \sigma^{(s)} \left(-\nabla \phi^{(s)} + \mathbf{u}^{(s)} \times \mathbf{B} \right). \tag{22}$$

If the Hall effect is retained, Eq. (22) is replaced by the tensor form obtained from Eq. (11). The scalar-conductivity form is used here for robustness and for consistency with the reference OREX setup. Cell-centered $\mathbf{J} \times \mathbf{B}$ and the electromagnetic energy source are evaluated from Eq. (16).

3.3 Gas-dynamic update and strong coupling

The conservative variables are advanced by solving

$$\left[\frac{\Omega_j}{\Delta \tau} \mathbf{I} + \frac{\partial \mathbf{R}_j^c}{\partial \mathbf{U}} \right] \Delta \mathbf{U}_j = -\mathbf{R}_j^c - \mathbf{R}_j^n + \Omega_j \left(\mathbf{S}_j^{chem} + \mathbf{S}_j^{em} \right), \tag{23}$$

where $\Delta \tau$ is the local pseudo-time step. The NCCR residual and electromagnetic source terms are treated explicitly within each coupling sub-iteration and updated repeatedly. Strong-field cases use an under-relaxed source update,

$$\mathbf{S}_{em}^{(s)} \leftarrow (1 - \alpha_M) \mathbf{S}_{em}^{(s-1)} + \alpha_M \mathbf{S}_{em}^{(s)}, \tag{24}$$

with $0 < \alpha_M \leq 1$. This relaxation suppresses abrupt $\mathbf{J} \times \mathbf{B}$ variations in cells where σ changes rapidly with T_t, T_v, and n_e.

The coupling sequence follows the modular treatment often used in nonequilibrium ionized-flow simulations with electromagnetic fields [31]:

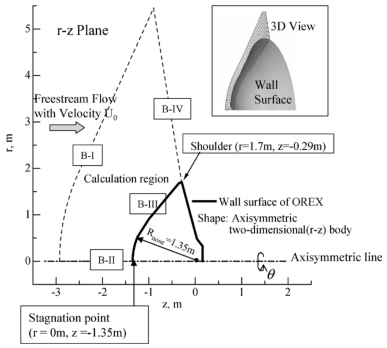
1. Given $\mathbf{U}^n$, set $\mathbf{U}^{(0)} = \mathbf{U}^n$ and initialize the electromagnetic source from the previous pseudo-time step.
2. From $\mathbf{U}^{(s)}$, update p, T_t, T_v, Y_i, transport coefficients, reaction rates, n_e, and σ. Positivity of density, temperature, and species mass fraction is enforced before chemical and electromagnetic properties are evaluated.
3. Solve the local NCCR closure in every cell using Eqs. (18)–(20). Assemble the NCCR stress, excess normal stress, heat flux, and species diffusion contributions to $\mathbf{R}_j^n$.
4. Solve the variable-coefficient potential equation, Eq. (21). Reconstruct $\mathbf{E}$ and $\mathbf{J}$, and compute $\mathbf{J} \times \mathbf{B}$ and $\mathbf{J} \cdot \mathbf{E}$.
5. Assemble Eq. (23) and advance the gas-dynamic variables. The updated velocity, T_t, and T_v modify $\mathbf{u} \times \mathbf{B}$, σ, and NCCR fluxes in the next sub-iteration.
6. Correct the species mass fractions so that $\sum_i Y_i = 1$, update the two-temperature energy exchange, and recompute mixture thermodynamics.
7. Repeat steps 2–6 until the coupled change satisfies

$$\max \left(\frac{\left\| \mathbf{U}^{(s+1)} - \mathbf{U}^{(s)} \right\|}{\left\| \mathbf{U}^{(s)} \right\| + \varepsilon_U}, \frac{\left\| \phi^{(s+1)} - \phi^{(s)} \right\|}{\left\| \phi^{(s)} \right\| + \varepsilon_\phi}, \frac{\left\| \mathbf{W}^{(s+1)} - \mathbf{W}^{(s)} \right\|}{\left\| \mathbf{W}^{(s)} \right\| + \varepsilon_W} \right) < \varepsilon_C. \tag{25}$$

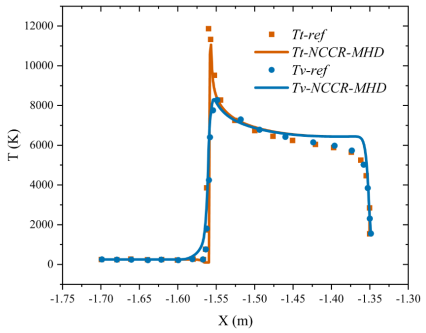
Physically, the NCCR gas-dynamic solver provides the shock-layer flow gradients and nonequilibrium transport fluxes; the thermochemical state determines n_e and σ. The electromagnetic solver computes $\mathbf{J}$ driven by $-\nabla \phi + \mathbf{u} \times \mathbf{B}$. The Lorentz force, $\mathbf{J} \times \mathbf{B}$, decelerates the conducting post-shock plasma and changes the bow-shock standoff distance; Joule heating feeds back into the total energy and T_v equations. Replacing the local NCCR iteration with the constitutive relation in Eq. (9) reduces the model to an NSF-MHD solver, which serves as a reference for separating rarefaction effects from purely electromagnetic coupling effects.

4. Validation Case

The method is first validated using the OREX configuration at $H = 59.6$ km, with comparison against the numerical MHD flow control results of Fujino and Ishikawa [8]. Fig. 1 shows the computational geometry, boundary conditions, and stagnation-line temperature distributions. This case is used to examine whether, before the RAM-C II parametric study, the coupled solver can reasonably predict the shock-layer thermal nonequilibrium and pressure response produced by the imposed magnetic field.



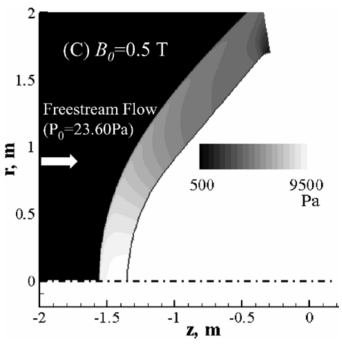
(a) Geometry and boundary conditions.



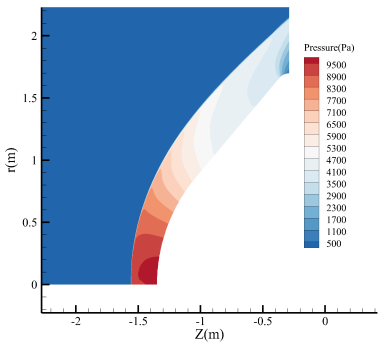
(b) Stagnation-line temperatures.

Figure 1 – OREX validation case used for assessing the NCCR-MHD solver.

The pressure contours in Fig. 2 agree well with the reference calculation in the compressed forebody region and in the overall pressure distribution. Together with the stagnation-line temperature profiles, this comparison shows that the present solver captures the main gas-dynamic response induced by the electromagnetic source term, supporting its use in the subsequent analysis of shock displacement and thermal loading.



(a) Reference result [8].



(b) Present NCCR-MHD simulation.

Figure 2 – Pressure contours for the OREX case at $H = 59.6$ km and $B_0 = 0.5$ T.

5. Results and Discussion

All application cases use the RAM-C II axisymmetric blunt sphere-cone shown in Fig. 3. Unless otherwise stated, the thermochemical gas model is Park's two-temperature model with an 11-species finite-rate air chemistry mechanism, and the imposed magnetic field follows the dipole distribution given in Eq. (14).

Fig. 4 sketches the MHD thermal protection mechanism considered in this study. In the weakly ionized shock layer, the interaction between the imposed magnetic field and the induced current density $\mathbf{J}$ produces the Lorentz force $\mathbf{J} \times \mathbf{B}$, acting mainly on the post-shock gas ahead of the forebody. This force extracts axial momentum, pushes the bow shock upstream, modifies the near-wall streamline pattern, and changes the heat transport path to the wall.

Only two operating parameters are varied in this section: flight altitude H and stagnation-point magnetic flux density B_0. With the vehicle geometry, gas model, and magnetic field topology fixed, their

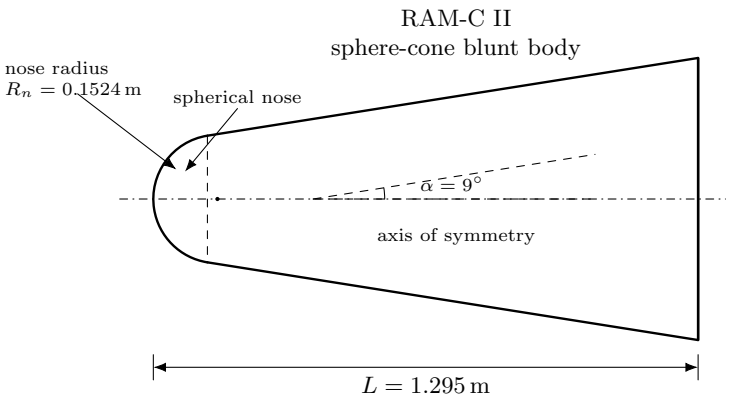


Figure 3 – Schematic of the RAM-C II sphere-cone blunt-body geometry used in the application cases.

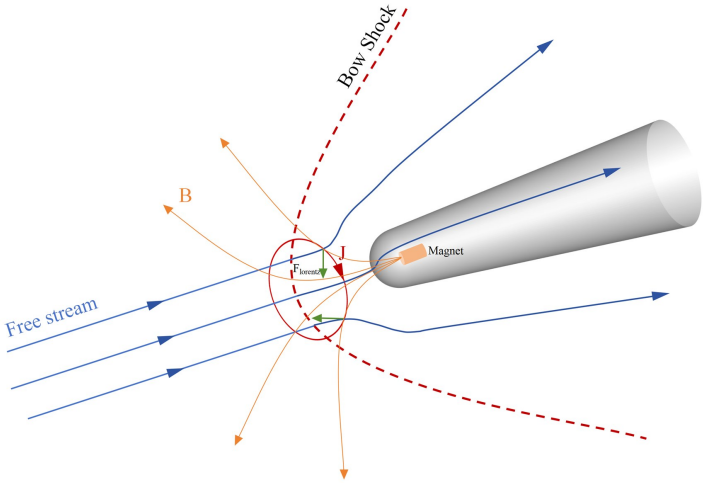


Figure 4 – Schematic of the MHD thermal protection mechanism around the RAM-C II blunt body.

effects on MHD thermal protection and the associated flowfield structure can be examined separately.

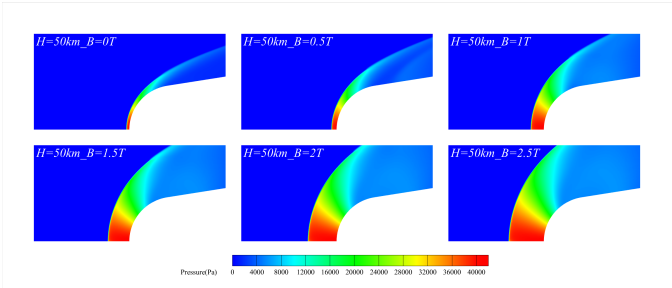
5.1 Effect of Stagnation-Point Magnetic Flux Density

The B_0 sweep is performed at fixed freestream conditions, with $M_\infty = 20$ and $H = 50$ km. As listed in Table 1, the stagnation-point magnetic flux density B_0 ranges from 0 to 2.5 T. For this set of cases, the freestream state is unchanged, and B_0 is the primary control parameter.

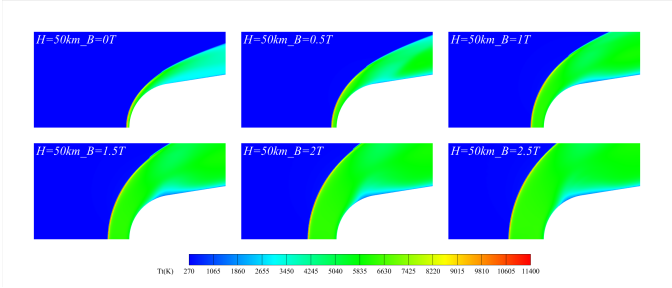
Table 1 – Computational conditions for the magnetic flux density sweep.

Operating condition	Value
Freestream Mach number, M_∞	20
Flight altitude, H	50 km
Stagnation-point magnetic flux density, B_0	0, 0.5, 1.0, 1.5, 2.0, and 2.5 T

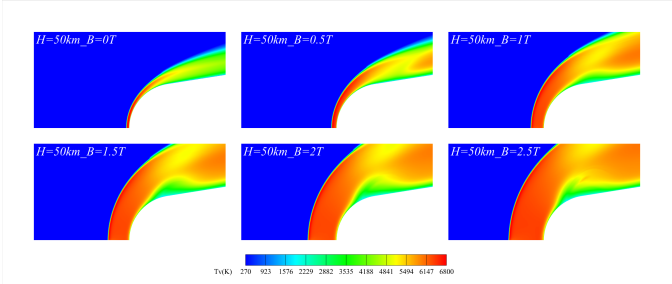
Fig. 5 shows the p, T_t, and T_v fields for different values of B_0. The p contours in Fig. 5a show that the incoming hypersonic flow is compressed by the detached bow shock, forming a high-pressure region behind the shock. As B_0 increases, this high-pressure region expands upstream and laterally, giving the magnetic drag-parachute structure commonly observed in blunt-body MHD studies [6, 7]. This behavior is not simply a geometric outward displacement of the shock. The electromagnetic body force extracts axial momentum from the conducting post-shock plasma, increases the effective resistance ahead of the vehicle, and distributes the pressure load over a thicker shock layer.



(a) Pressure contours.



(b) T_t contours.



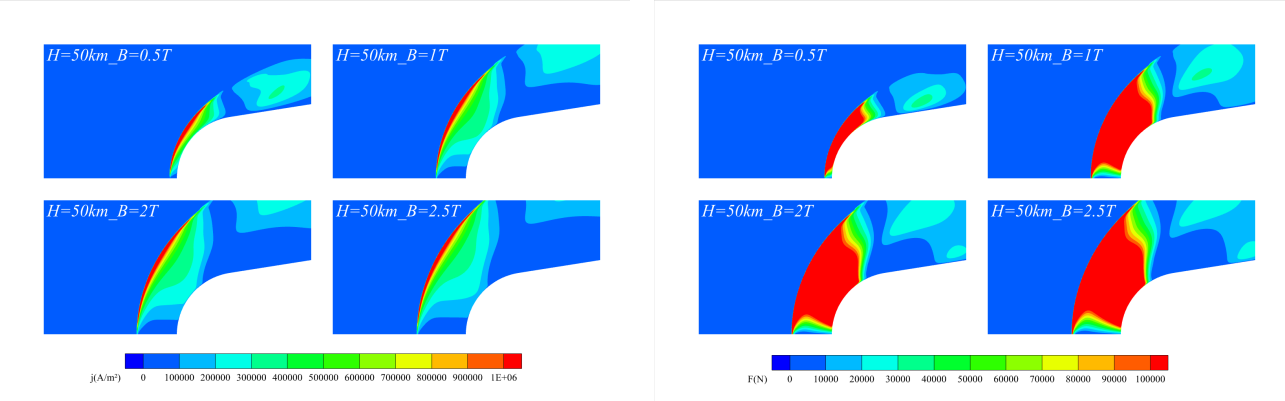
(c) T_v contours.

Figure 5 – Two-dimensional pressure and temperature contours for the magnetic flux density sweep at $H = 50$ km and $M_\infty = 20$.

The T_t and T_v fields in Figs. 5b and 5c reveal the thermochemical nonequilibrium process underlying the pressure response. The peak T_t remains close to the bow shock, where the freestream kinetic energy is first converted into internal modes. By contrast, the T_v field is smoother and shows a clear spatial lag; finite-rate vibrational relaxation cannot follow the rapid post-shock compression instantaneously. As the bow shock moves away from the nose, the high-temperature region is also lifted from the wall. The thicker thermal buffer reduces the wall-normal temperature gradient near the stagnation line, and the nose heat load decreases accordingly.

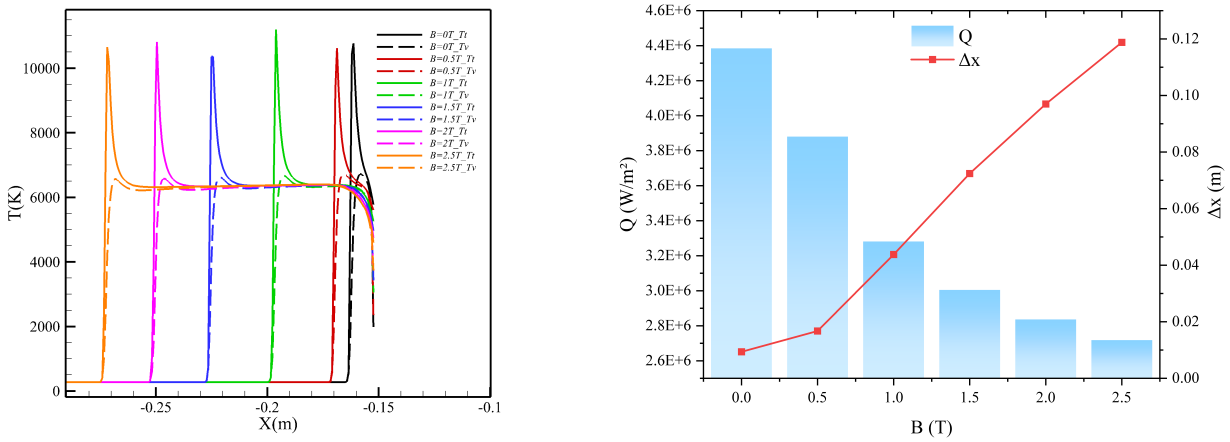
Fig. 6 shows the corresponding electromagnetic source terms and identifies the region responsible for the heat-flux redistribution. The current density $\mathbf{J}$ is driven by the motional electric field and the electric-potential gradient in the conducting post-shock plasma. It is mainly confined to the shock-layer region where high temperature, electron production, and appreciable σ overlap. The Lorentz force source term $\mathbf{J} \times \mathbf{B}$ has a similar spatial envelope. As B_0 increases, its magnitude rises markedly and the active region shifts upstream. The strongest braking occurs behind the detached shock rather than near the wall. Axial momentum is extracted before the gas reaches the stagnation point, thickening the shock layer and weakening the near-wall thermal gradient.

The stagnation-line profiles in Fig. 7 show the same trend: the T_t jump moves upstream and the relaxation zone broadens under magnetic interaction. The shock standoff distance increases rapidly with B_0. Relative to the zero-field case, the increase is 78.28% at $B_0 = 0.5$ T and reaches 1165.11% at $B_0 = 2.5$ T, for which the standoff distance is about 12.65 times the baseline value.



(a) $|\mathbf{J}|$, A/m^2. (b) $|\mathbf{J}\times\mathbf{B}|$, N/m^3.

Figure 6 – $\mathbf{J}$ and $\mathbf{J}\times\mathbf{B}$ contours for different stagnation-point magnetic flux densities at $H = 50$ km and $M_\infty = 20$.



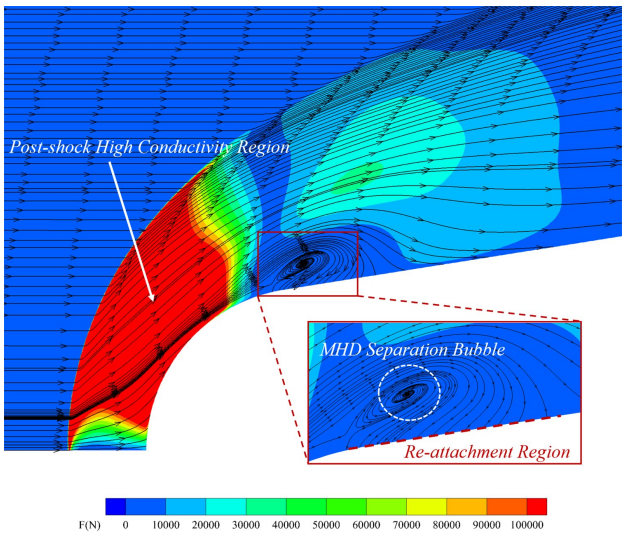
(a) Stagnation-line temperatures. (b) Stagnation-point heat flux and shock standoff distance.

Figure 7 – Stagnation-line thermal response under different magnetic flux densities at $H = 50$ km and $M_\infty = 20$.

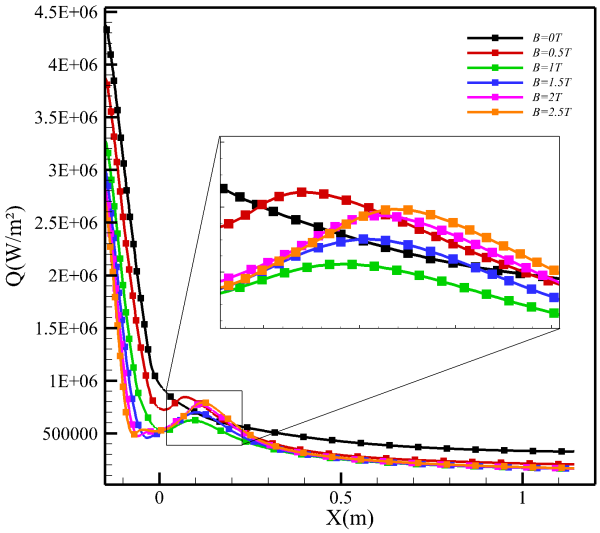
The stagnation-point magnetic flux density strongly affects the shock standoff distance, while its influence on stagnation-point heat flux is more limited. As shown in Fig. 7b, the stagnation-point heat flux decreases monotonically with B_0, from 4.384×10^6 W/m^2 in the zero-field case to 2.718×10^6 W/m^2 at $B_0 = 2.5$ T. This corresponds to a 38.01% reduction and is consistent with the saturation behavior discussed by Bityurin and Bocharov [9]. MHD thermal protection performance is not controlled solely by shock displacement: thermal conduction, diffusive transport, thermochemical relaxation, and electromagnetic energy deposition remain active within the enlarged shock layer. Magnetic braking increases the energy-dissipation length scale ahead of the vehicle, while the high-temperature plasma layer can still conduct and diffuse heat toward the wall.

A reduction in stagnation-point heat flux does not imply a simultaneous decrease of the heat load over the entire surface. Once the shock layer expands, $\mathbf{J}\times\mathbf{B}$ becomes strongly nonuniform along the wall and may reorganize the shoulder flow. Fig. 8 compares the local electromagnetic body-force distribution with the corresponding wall heat flux response.

The conducting post-shock plasma forms a localized $\mathbf{J}\times\mathbf{B}$ region that pushes the bow shock away from the nose. Near the shoulder, the same electromagnetic force system modifies the streamwise pressure gradient. Local deceleration and pressure rise promote boundary-layer separation, producing a magnetically induced recirculation bubble, as shown in Fig. 8a. The wall heat flux profiles in Fig. 8b show the direct consequence of this flow reorganization. As B_0 increases, the nose heat flux decreases; stronger fields, however, make the shoulder heat flux peak more pronounced. The magnetic field does not simply suppress convective heating. It redistributes the active regions of



(a) $\mathbf{J} \times \mathbf{B}$ contours and induced vortex at $B_0 = 1$ T.

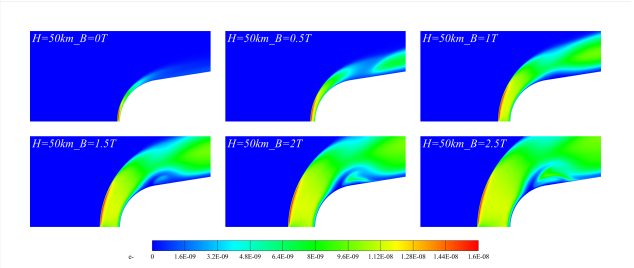


(b) Wall heat flux distributions under different B_0.

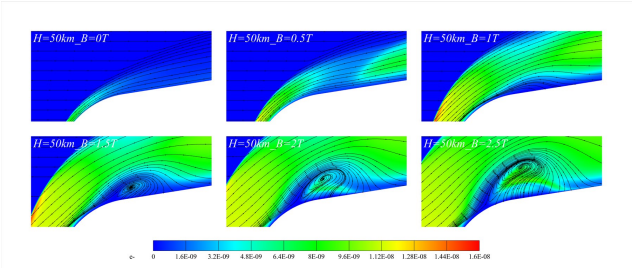
Figure 8 – Local MHD-induced flow redistribution and the associated wall heat flux response at $H = 50$ km and $M_\infty = 20$.

momentum extraction, appreciable σ, and electromagnetic energy deposition. Beyond a certain magnetic flux density, the additional cooling gained at the nose is partly offset by enhanced reattachment heating.

The n_e contours in Fig. 9 explain the local nature of this feedback. Ionization occurs mainly in the high-temperature post-shock layer. The $\mathbf{J}$ and $\mathbf{J} \times \mathbf{B}$ fields peak only where electron-rich gas, the motional electric field, and the imposed magnetic field overlap in space. The vortex-resolved contours show that the separated shoulder flow traps part of the conducting plasma and convects it toward the reattachment region. Downstream of the recirculation bubble, the local σ increases, allowing $\mathbf{J}$, Joule heating, and shear-layer impingement to reinforce one another. This leads to a practical saturation of MHD thermal protection efficiency: design assessment should consider the integrated forebody heat load rather than the minimum stagnation-point heat flux alone.



(a) n_e contours.



(b) n_e redistribution around the magnetically induced vortex.

Figure 9 – n_e contours highlighting the coupling between ionization, σ, and shoulder-region vortex transport.

5.2 Effect of Flight Altitude

The altitude sweep uses the same geometry, thermochemical model, and dipole magnetic field definition. At each altitude listed in Table 2, the zero-field case and the $B_0 = 1$ T case are computed and compared.

The p fields in Fig. 10 show two altitude-dependent features. Without a magnetic field, the detached shock remains close to the forebody, and the high-pressure region is mainly confined near the nose. With $B_0 = 1$ T, the compressed region expands upstream and laterally; this expansion becomes more

Table 2 – Computational conditions for the altitude sweep.

Operating condition	Value
Freestream Mach number, M_∞	20
Flight altitude, H	30, 40, 50, 60, and 70 km
Stagnation-point magnetic flux density, B_0	0 and 1.0 T

evident over 50–70 km. Flight altitude changes not only the absolute pressure level, but also the effective volume over which the electromagnetic body force redistributes momentum within the shock layer.

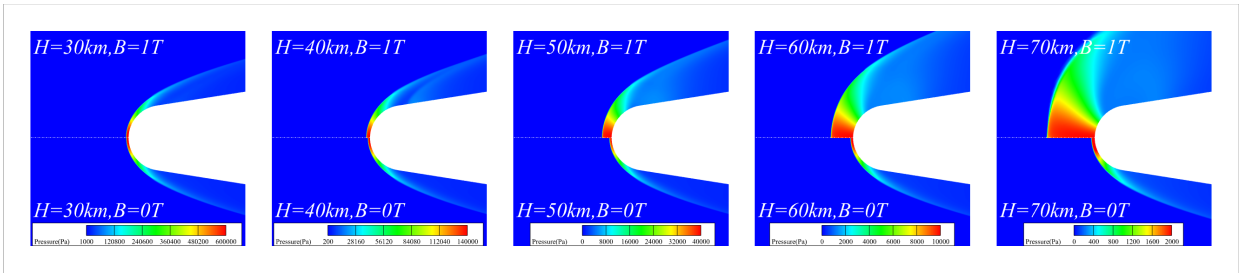


Figure 10 – p contours at different altitudes for zero-field and magnetic field cases at $M_\infty = 20$; the magnetic field contours use $B_0 = 1$ T.

The n_e contours in Fig. 11 explain why the magnetic response becomes stronger at higher altitude. At lower altitude, the electron-rich region is thin and remains mainly close to the bow shock and forebody. As altitude increases, the shock layer thickens and the ionized region occupies a larger portion of the layer. Under the action of the magnetic field, the conducting plasma is further lifted from the wall and stretched along the shock layer. The increased spatial overlap between the region with finite n_e and the imposed magnetic field provides a larger current-carrying medium for Lorentz-force braking. This trend is consistent with the OREX observation that MHD thermal protection is most effective when natural shock-layer ionization is sufficient to sustain electric current [8].

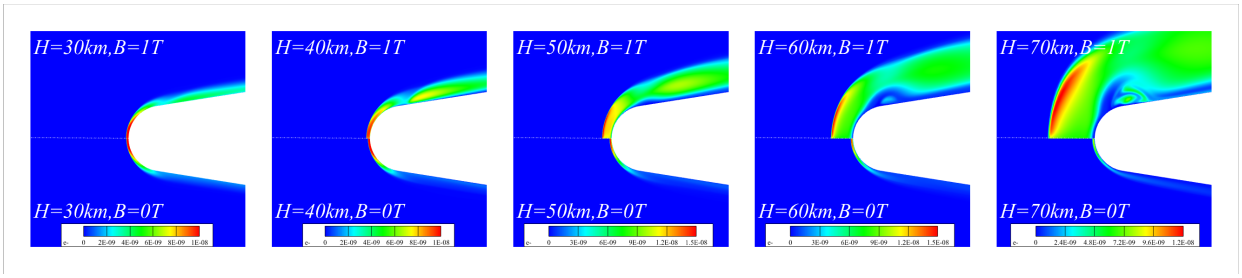
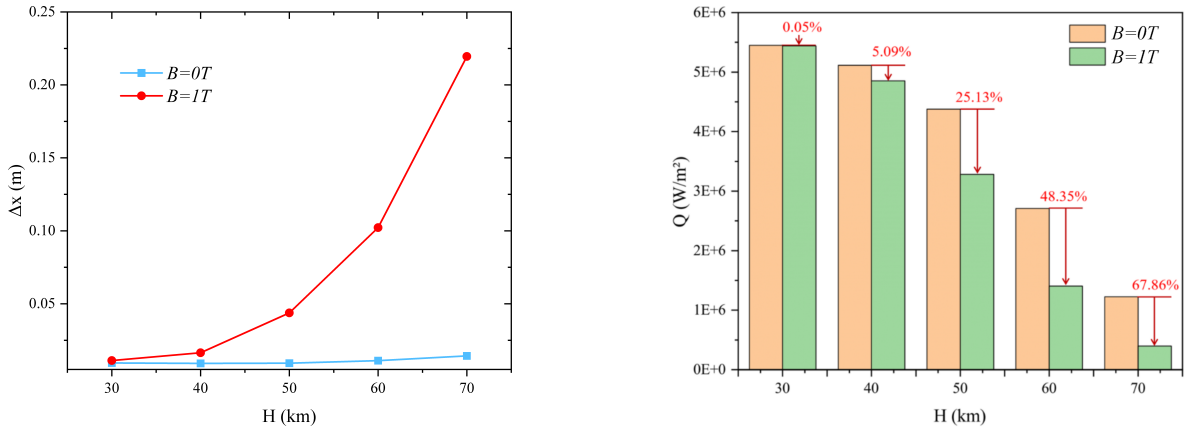


Figure 11 – n_e contours at different altitudes for zero-field and magnetic field cases at $M_\infty = 20$; the magnetic field contours use $B_0 = 1$ T.

The shock standoff distances in Fig. 12a quantify the above change in flow structure. Without a magnetic field, the standoff distance remains small and varies only weakly with altitude. With $B_0 = 1$ T, the magnetic response is still weak over 30–40 km; above about 50 km, the upstream displacement of the shock becomes much more pronounced. The standoff distance is approximately 0.10 m at 60 km and increases to about 0.22 m at 70 km. The imposed field therefore does not produce the same degree of shock displacement at all altitudes. Effective upstream shock motion requires a sufficiently thick current-carrying shock layer with appreciable ionization.

The stagnation-point heat flux shows a similar altitude dependence. For $B_0 = 1$ T, the heat-flux reduction at 30 km is almost negligible, only 0.05% relative to the zero-field baseline; at 40 km, the reduction remains limited. At 50 km, the reduction reaches 25.13%, increasing to 48.35% at 60 km and 67.86% at 70 km. The close correspondence between heat-flux reduction and standoff growth indicates that this MHD control configuration is more effective at higher altitude. The wall heat flux profiles in Fig. 13



(a) Shock standoff distance.

(b) Stagnation-point heat flux.

Figure 12 – Shock standoff distance and stagnation-point heat flux versus flight altitude for zero-field and $B_0 = 1$ T magnetic field cases.

also become smoother as altitude increases, with a weaker shoulder heat flux penalty. This result suggests an early-activation strategy: applying MHD control at higher altitude can reduce the initial thermal load, increase electromagnetic drag, and lower the vehicle speed before entry into denser atmospheric layers, where the margin of the passive TPS is more restrictive.

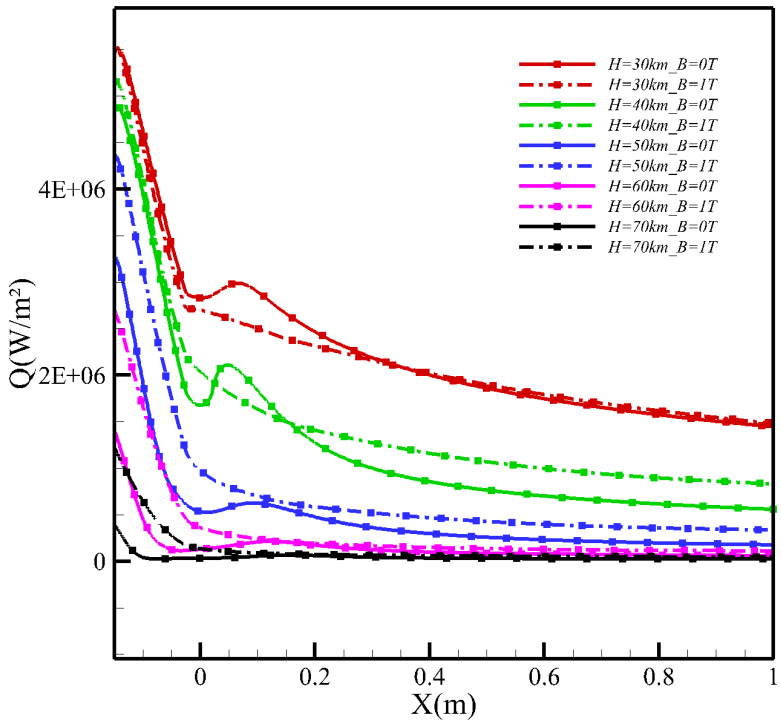


Figure 13 – Wall heat flux distributions at different flight altitudes for zero-field and $B_0 = 1$ T magnetic field cases.

6. Conclusions

A finite-volume solver for hypersonic weakly ionized air plasma flows is developed. It couples multi-component NCCR transport with the reduced Maxwell equations and includes two-temperature thermochemistry, finite-rate multicomponent reactions, finite electrical conductivity σ, induced current density $\mathbf{J}$, Lorentz forcing $\mathbf{J} \times \mathbf{B}$, and electromagnetic energy deposition. Its predictive capability is assessed against OREX numerical data.

For the RAM-C II configuration, increasing the stagnation-point magnetic flux density pushes the bow

shock upstream, increases the shock standoff distance, and reduces the stagnation-point heat flux by lengthening the energy-dissipation path ahead of the nose. At $H = 50$ km and $M_\infty = 20$, increasing B_0 from 0 to 2.5 T increases the standoff distance to 12.65 times the zero-field value and reduces the stagnation-point heat flux by 38.01%. For $B_0 = 1$ T, the heat-flux reduction increases from 0.05% at 30 km to 67.86% at 70 km, with the standoff distance increasing to approximately 0.22 m.
The p, T_t, T_v, $\mathbf{J}$, $\mathbf{J} \times \mathbf{B}$, and n_e fields show that the MHD thermal-protection response is governed mainly by the redistribution of the conducting post-shock plasma, rather than by magnetic-field strength alone. Strong magnetic fields may also reorganize the shoulder flow, confine electron-rich gas within the separation bubble, and enhance local reattachment heating. Flight altitude affects MHD thermal-protection performance by changing the available current-carrying volume. At higher altitude, the shock layer is more favorable for an extended Lorentz-force braking region, giving larger heat-flux reduction and smoother wall heat flux distributions. The value of B_0 and the activation altitude should therefore be selected together, balancing stagnation-point cooling, increased shoulder heat load, and aerodynamic deceleration associated with magnetic drag.

7. Contact Author Email Address

Contact author: shihao302@mail.nwpu.edu.cn

8. Copyright Statement

The authors confirm that they, and/or their company or organization, hold copyright on all of the original material included in this paper. The authors also confirm that they have obtained permission, from the copyright holder of any third party material included in this paper, to publish it as part of their paper. The authors confirm that they give permission, or have obtained permission from the copyright holder of this paper, for the publication and distribution of this paper as part of the ICAS proceedings or as individual off-prints from the proceedings.

References

[1] John D. Anderson. *Hypersonic and High-Temperature Gas Dynamics*. American Institute of Aeronautics and Astronautics, Reston, VA, 2 edition, 2006.
[2] Walter G. Vincenti and Charles H. Kruger. *Introduction to Physical Gas Dynamics*. John Wiley and Sons, New York, 1965.
[3] Chul Park. *Nonequilibrium Hypersonic Aerothermodynamics*. John Wiley and Sons, New York, 1990.
[4] J. A. Fay and F. R. Riddell. Theory of stagnation point heat transfer in dissociated air. *Journal of the Aeronautical Sciences*, 25(2):73–85, 1958.
[5] P. O. Jarvinen and R. H. Adams. The aerodynamic characteristics of large angled cones with retrorockets. In *AIAA Paper 70-583*, 1970.
[6] William B. Bush. Magnetohydrodynamic-hypersonic flow past a blunt body. *Journal of the Aerospace Sciences*, 25(11):685–690, 1958.
[7] Klaus A. Hoffmann, Henri-Marie Damevin, and Jean-Francois Dietiker. Numerical simulation of hypersonic magnetohydrodynamic flows. In *31st AIAA Plasmadynamics and Lasers Conference*, Denver, Colorado, 2000. AIAA Paper 2000-2259.
[8] Takayasu Fujino and Motoo Ishikawa. Numerical simulation of control of plasma flow with magnetic field for thermal protection in earth reentry flight. *IEEE Transactions on Plasma Science*, 34(2):409–420, 2006.
[9] V. A. Bityurin and A. N. Bocharov. MHD heat flux mitigation in hypersonic flow around a blunt body with ablating surface. *Journal of Physics D: Applied Physics*, 51:264001, 2018.
[10] Alexis Lefevre, David E. Gildfind, Rowan J. Gollan, Peter A. Jacobs, Timothy J. McIntyre, and Christopher M. James. Expansion tube experiments of magnetohydrodynamic aerobraking for superorbital earth reentry. *AIAA Journal*, 59(8), 2021.
[11] Heather A. Muir and Nikos Nikiforakis. Numerical modeling of imposed magnetohydrodynamic effects in hypersonic flows. *Physics of Fluids*, 34(10):107114, 2022.
[12] Kai Luo, Qiu Wang, Jinping Li, Wei Zhao, and Sangdi Gu. A quasi-one-dimensional model for the stagnation streamline in hypersonic magnetohydrodynamic flows. *Physics of Fluids*, 35(3):036101, 2023.
[13] Hao Jiang, Jun Liu, Xueke Che, Yang Du, Wei Huang, Feng Ding, and Tiantian Zhang. Magnetic field control of high-enthalpy shock wave/boundary-layer interactions using a fully implicit thermochemical non-equilibrium solver. *Aerospace Science and Technology*, 143:108507, 2023.
[14] Vatsalya Sharma, Vincent F. Giangaspero, Stefaan Poedts, and Andrea Lani. Influence of magnetohydrodynamics configuration on aerothermodynamics during martian reentry. *Physics of Fluids*, 36(3):036115, 2024.
[15] Thomas J. Greenslade, Arun Kumar Chinnappan, and Minkwan Kim. Multi-physics simulation study of magnetic shielding on hypersonic vehicles. *CEAS Space Journal*, 17(4):549–560, 2024.
[16] Johannes W. Oswald, Andrea Lani, and Georg Herdrich. Experimental investigation on MHD flow manipulation in high enthalpy air plasma. *Vacuum*, 236:114565, 2025.
[17] G. A. Bird. *Molecular Gas Dynamics and the Direct Simulation of Gas Flows*. Clarendon Press, Oxford, 1994.
[18] Iain D. Boyd, Gang Chen, and Graham V. Candler. Predicting failure of the continuum fluid equations in transitional hypersonic flows. *Physics of Fluids*, 7(1):210–219, 1995.
[19] R. S. Myong. Thermodynamically consistent hydrodynamic computational models for high-Knudsen-number gas flows. *Physics of Fluids*, 11(9):2788–2802, 1999.
[20] R. S. Myong. Coupled nonlinear constitutive models for rarefied and microscale gas flows: subtle interplay of kinematics and dissipation effects. *Continuum Mechanics and Thermodynamics*, 21:389–399, 2009.
[21] J. W. Ahn and C. Kim. An axisymmetric computational model of generalized hydrodynamic theory for rarefied multi-species gas flows. *Journal of Computational Physics*, 228(11):4088–4117, 2009.

[22] Zhongzheng Jiang, Wenwen Zhao, Zhenyu Yuan, Weifang Chen, and R. S. Myong. Computation of hypersonic flows over flying configurations using a nonlinear constitutive model. *AIAA Journal*, 57(12), 2019.
[23] Shuhua Zeng, Zhiqiang He, Wenwen Zhao, and Weifang Chen. A computational strategy for nonlinear coupled constitutive relations of rarefied nonequilibrium flows on unstructured grids. *Aerospace Science and Technology*, 141:108477, 2023.
[24] Shuhua Zeng, Zhenyu Yuan, Wenwen Zhao, and Weifang Chen. Numerical simulation of hypersonic thermochemical nonequilibrium flows using nonlinear coupled constitutive relations. *Chinese Journal of Aeronautics*, 36(3):63–79, 2023.
[25] Shuhua Zeng, Junyuan Yang, Wenwen Zhao, Zhenyu Yuan, Guochao Fan, and Weifang Chen. Nonlinear coupled constitutive relations for hypersonic reacting flows with thermal nonequilibrium effect. *Physics of Fluids*, 37(1), 2025.
[26] Chul Park. Review of chemical-kinetic problems of future NASA missions. I: Earth entries. *Journal of Thermophysics and Heat Transfer*, 7(3):385–398, 1993.
[27] F. G. Blottner, M. Johnson, and M. Ellis. Chemically reacting viscous flow program for multi-component gas mixtures. Technical Report SC-RR-70-754, Sandia Laboratories, 1971.
[28] C. R. Wilke. A viscosity equation for gas mixtures. *The Journal of Chemical Physics*, 18(4):517–519, 1950.
[29] Roop N. Gupta, Jerrold M. Yos, Richard A. Thompson, and Kam-Pui Lee. A review of reaction rates and thermodynamic and transport properties for an 11-species air model for chemical and thermal nonequilibrium calculations to 30000 K. Reference Publication NASA-RP-1232, NASA, 1990.
[30] Peter A. Gnoffo, Roop N. Gupta, and Judy L. Shinn. Conservation equations and physical models for hypersonic air flows in thermal and chemical nonequilibrium. Technical Paper NASA-TP-2867, NASA, 1989.
[31] Robert W. MacCormack. Non-equilibrium ionized flow simulations within strong electro-magnetic fields. In *48th AIAA Aerospace Sciences Meeting Including the New Horizons Forum and Aerospace Exposition*, Orlando, Florida, 2010. AIAA Paper 2010-0225.
[32] P. L. Roe. Approximate Riemann solvers, parameter vectors, and difference schemes. *Journal of Computational Physics*, 43(2):357–372, 1981.
[33] Bram van Leer. Towards the ultimate conservative difference scheme. V. a second-order sequel to Godunov's method. *Journal of Computational Physics*, 32(1):101–136, 1979.
[34] Meng-Sing Liou. A sequel to AUSM: AUSM+. *Journal of Computational Physics*, 129(2):364–382, 1996.